XLI CILAMCE
XLI Ibero-Latin American Congress on Computational Methods in Engineering
16-19 November, 2020 FOZ DO IGUAÇU PARANÁ - BRAZIL

Calibration of a ductile damage model dependent on triaxiality and Lode angle parameter

Iago S. Santos, Diego. F. B. Sarzosa

Dept. of Naval and Oceanic Engineering, University of São Paulo
2231 Professor Mello Moraes Avenue, 05508-030, São Paulo, Brazil
iagosantos@usp.br, dsarzosa@usp.br

Abstract. This paper presents a numerical study using the Finite Element Method (FEM) to model the ductile fracture in ASTM A285 Gr. C steel through calibration of a phenomenological damage model. The calibrated damage model is composed of a damage initiation criterion dependent on the stress triaxiality and the Lode angle parameter coupled with a post-initiation damage evolution law. A series of experimental tests on round bars having smooth and notched cross-section, flat notched specimens under axial tensile loads, and fracture toughness tests in deeply cracked bending specimens SE(B) were carried out to calibrate the elastoplastic response and the damage parameters. Verification of the calibrated parameters is performed using a SE(B) sample having a shallow crack size ratio. The agreement between the experimental tests and the numerical model results is quite good. The adopted numerical procedure can be used to predict the response of a more complex structure.

Keywords: ductile fracture, damage model, triaxiality, Lode angle.

1 Introduction

The understanding of the mechanisms of ductile fracture has been the subject of many studies due to the possibilities of application in the various fields of industry. In critical engineering structures such as pipelines, pressure vessels, ships, and aircraft, the ductile fracture is an important failure mode to be verified in the design and operation phases. Computational damage models are used to obtain accurate results in the prediction of the ductile fracture without the need for a large number of experimental tests.

Damage models are proposed in order to link field variables (stress, deformation, triaxiality, etc.) to the evolution of damage in the material through a weighting function phenomenological defined (empirical) or based on micromechanical observations of ductile fracture mechanisms, such as void nucleation, growth, and coalescence [1]. These models are commonly classified as uncoupled or coupled as to the coupling of the field variable to the material constitutive equations.

Uncoupled models assume that the damage process is independent of the material plastic behavior, assuming that the damage to which the body is subjected does not influence the stress and strain states. They predict the fracture to occur when an external control variable, commonly represented by a scalar field, reaches a critical value [2]. In the coupled models, the material plastic properties are considered a function of the accumulated damage, causing changes in the microstructure of the material during the fracture process [2]- [3]. From the physical point of view, the adoption of this coupling occurs due to the nature of the damage, in which its advance results in the appearance of microvoids and microcracks related to the reduction of stiffness of the solid. In this paper, a phenomenological approach is used to study the ductile failure of a typical pressure vessel steel. An uncoupled fracture initiation criterion is calibrated by using the Modified Mohr-Coulomb (MMC) criterion and the damage-induced softening is introduced in the post-initiation fracture.

The calibration of the initiation criterion is performed through experimental tests and FE analysis of axisymmetric and plane strain specimens under uniaxial stress. The softening law coefficients calibration and the damage model validation are performed through fracture toughness tests.

2 Stress States Characterization

The plasticity theory demonstrates that the mechanical properties of isotropic materials are independent of the rotation of the adopted coordinate system [4]. Therefore, a stress tensor σ_{ij} written as a function of principal stresses σ_1, σ_2, and σ_3 can be used to represent the stress state at any point of the body [5].

$$\sigma_{ij} = S_{ij} + p. \tag{1}$$

where p is the mean or hydrostatic stress, related to the first invariant of Cauchy stress tensor, I_1

$$p = \sigma_m = \frac{I_1}{3} = \frac{(\sigma_1+\sigma_2+\sigma_3)}{3}. \tag{2}$$

and S_{ij} is the deviator tensor. The second and third invariants (J_2 and J_3, respectively) are given by

$$q = \bar{\sigma}_{eq} = \sqrt{3J_2} = \sqrt{\frac{[(\sigma_1-\sigma_2)^2+(\sigma_2-\sigma_3)^2+(\sigma_3-\sigma_1)^2]}{2}}. \tag{3}$$

$$r = \left[\frac{27J_3}{2}\right]^{(1/3)} = \left[\frac{27}{2}(\sigma_1-\sigma_m)(\sigma_2-\sigma_m)(\sigma_3-\sigma_m)\right]^{(1/3)}. \tag{4}$$

where $\bar{\sigma}_{eq}$ is the von Mises equivalent stress.

Damage models conveniently work with two dimensionless parameters to characterize a stress state: the first is called stress triaxiality η, corresponding to the normalization of hydrostatic stress by von Mises equivalent stress.

$$\eta = \frac{p}{q} = \frac{\sigma_m}{\bar{\sigma}_{eq}}. \tag{5}$$

The second parameter is the Lode angle θ, related to the normalized third stress invariant ξ by

$$\xi = \left(\frac{r}{q}\right)^3 = cos(3\theta). \tag{6}$$

From the equation above, note that θ is defined between the angles 0 and $\pi/3$, resulting in a range for ξ of -1 to 1. Furthermore, the Lode angle can be normalized by [5]

$$\bar{\theta} = 1 - \frac{6\theta}{\pi} = 1 - \frac{2}{\pi}arccos(\xi). \tag{7}$$

The range of $\bar{\theta}$ is $-1 \leq \bar{\theta} \leq 1$. The parameter $\bar{\theta}$ is called the Lode angle parameter. For some notable loading conditions, $\bar{\theta}$ assumes constant values, with $\bar{\theta} = 1$ corresponds to the axisymmetric tension, $\bar{\theta} = 0$ corresponds to the plane strain or generalized shear loading conditions and $\bar{\theta} = -1$ corresponds to the axisymmetric compression. Thus, all stress states can be characterized by the above defined set of parameters $(\eta, \bar{\theta})$ [5].

3 Damage model

3.1 Fracture initiation criterion

The fracture initiation surface will be constructed according to the Modified Mohr-Coulomb criterion (MMC) proposed by Bai and Wierzbicki [6]. The MMC criterion characterizes the ductile fracture of isotropic solids, where the fracture occurs according to a surface, when the combination of normal stress σ_n and shear stress τ reach a critical value. Bai and Wierzbicki [6] determined these values according to original Mohr-Coulomb (MC) criterion:

$$max(\tau + c_1\sigma_n) = c_2. \tag{8}$$

where c_1 and c_2 are the friction coefficient and the shear resistance, respectively. The original MC is transformed into a criterion based on local three-dimensional strain in order to predict the onset of the fracture in strain hardening materials. Thus, the material ductility is indicated by the equivalent plastic strain to fracture $\bar{\varepsilon}_f$ with respect to the stress tensor, represented by the parameters η and $\bar{\theta}$. A third material coefficient c_3 is introduced for the representation of the three-dimensional surface of $\bar{\varepsilon}_f$ [6].

$$\bar{\varepsilon}_f(\eta,\bar{\theta}) = \left\{\frac{A}{c_2}\left[c_3 + \frac{\sqrt{3}}{2-\sqrt{3}}(1-c_3)\left(sec\left(\frac{\bar{\theta}\pi}{6}\right)-1\right)\right]\left[\sqrt{\frac{1+{c_1}^2}{3}}cos\left(\frac{\bar{\theta}\pi}{6}\right)+c_1\left(\eta+\frac{1}{3}sin\left(\frac{\bar{\theta}\pi}{6}\right)\right)\right]\right\}^{-\frac{1}{n}}. \quad (9)$$

Because η and $\bar{\theta}$ parameters do not remain constant during incremental load application in numerical analysis, average values of η and $\bar{\theta}$ must be used in the MMC calibration, integrating the values obtained in each time step from the beginning of the simulation until the fracture initiation time.

3.2 Damage evolution

The damage evolution is governed by a softening law that defines the degradation of the material strength when the fracture initiation criterion is reached. For any time of the analysis after reached the criterion, the stress tensor is modified by a scalar that considers the evolution of the isotropic damage

$$\sigma = (1-D)\bar{\sigma}. \quad (10)$$

where D is the damage variable that measures the material degradation after initiation and $\bar{\sigma}$ is the effective stress tensor calculated in the current increment, representing the stresses that would exist in the material without damage. From the beginning of the analysis until the instant when the initiation criterion is reached, $D = 0$. The material completely loses its strength when $D = 1$ [7].

The damage evolution results in softening of the yield stress and elasticity degradation [7]. In Fig. 1, the solid curve represents the damaged response in stress-strain, while the dashed curve is the response without damage. The yield stress softening is indicated by the relation $D\bar{\sigma}$ and the elasticity degradation by $E(1-D)$, where E is the Young's Modulus. $\bar{\varepsilon}_f$ corresponds to equivalent plastic strain when $D = 1$.

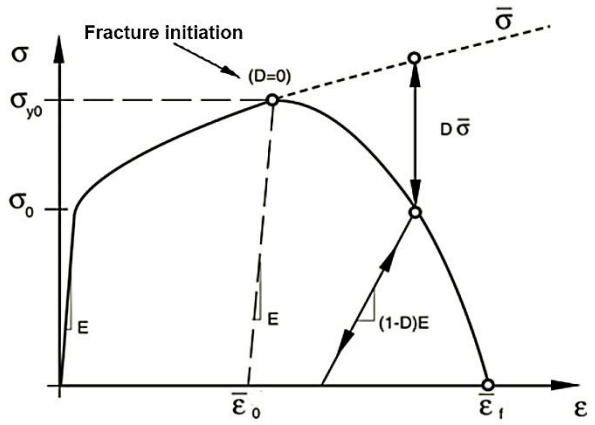

Figure 1. Effects of damage evolution on a stress-strain curve [7]

In this work, a model of exponential softening is adopted, requiring the calibration of two coefficients: the effective plastic displacement to fracture $\bar{u}_f^{pl}$ and the exponential softening factor m. The damage variable D is related to these parameters by:

$$D = \frac{1-e^{-\zeta(\bar{u}^{pl}/\bar{u}_f^{pl})}}{1-e^{-m}}. \quad (11)$$

4 Test procedure

4.1 Elastoplastic properties

The material investigated is the ASTM A285 grade C, a steel commonly used in melt welded pressure vessels. Uniaxial tests on smooth round bar specimens were performed by Cuenca and Sarzosa [8], and the test data were fitted to the model given by

$$\sigma = \begin{cases} E\varepsilon, & 0 \leq \varepsilon \leq \varepsilon_{el} \\ A(\varepsilon - \varepsilon_{el})^n, & \varepsilon > \varepsilon_{el}. \end{cases} \tag{12}$$

where σ is the true flow stress, ε is the true strain and ε_{el} is the elastic strain. The material properties are listed in Table 1. The insertion of plastic properties in Abaqus requires the supply of the true stress-strain curve of the material, shown in Fig. 2. σ_Y is the true yield stress of the material

Table 1. Elastoplastic properties for A285 Gr. C steel.

Material	**Density** (Kg/mm³)	E (GPa)	σ_y (MPa)	ν	A (MPa)	n
ASTM A285 Grade C	7.8E-09	207	306.15	0.3	860	0.21

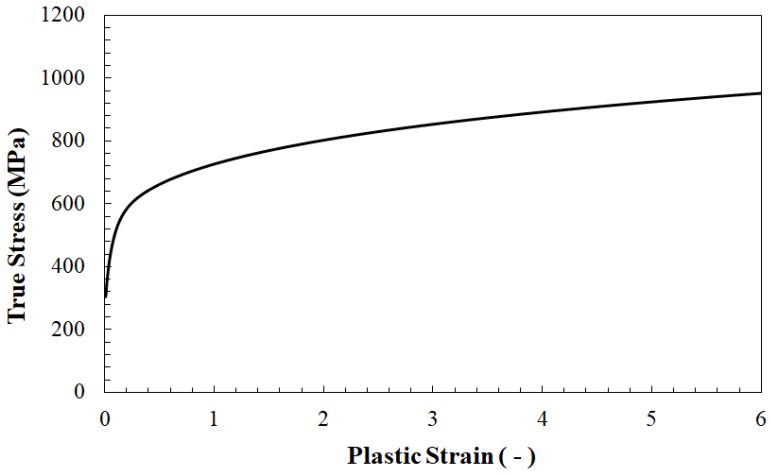

Figure 2. True stress-plastic strain curve of ASTM A285 steel

4.2 MMC criterion calibration

The calibration of the fracture initiation criterion was performed with the engineering stress-strain curves obtained by tensile tests of different specimens. The history of equivalent plastic strain was calculated at the potential fracture location. The equivalent plastic strain corresponding to the measured engineering strain at the time of the fracture was then considered as the $\bar{\varepsilon}_f$.

The tested specimens consisted of two notched round bars (NRB) and one flat grooved plate (FGP). The NRB are characterized by an axisymmetric state of stresses, corresponding to $\bar{\theta} = 1$ in uniaxial tensile tests. Fracture in these specimens occurs under ranges of high stress triaxiality ($\eta > 1/3$) [9]. Different values of the notch radius were considered to cover a wider range of η. FGP produce a plane strain state in the notch region, causing the specimen to fracture with $\bar{\theta} = 0$. These specimens also fracture under high stress triaxiality ranges. The Fig. 3 shows the main dimensions of the tested specimens.

FE models were developed in Abaqus/Explicit for reproduction of experimental engineering stress-strain curves. Due to symmetry, only $1/8$ of the geometries were modeled with appropriate constraints imposed on the symmetry planes. Eight-node brick element with reduced integration (C3D8R) were used in the simulations. The mesh constructed for the numerical analysis of the NRB2 and FGP are shown in Fig. 4. A mesh refinement in the notch region was adopted for improving the precision of the numerical results.

Good match between experimental and numerical engineering stress-strain curves were obtained, as shown in Fig. 5. For both tests, the numerical curves are not able to predict the fall of the experimental curves due to the absence of ductile fracture initiation criteria in the analysis.

Equivalent plastic strain, triaxiality and Lode angle parameter histories were obtained through numerical analyses mapping the critical element of the specimens, considered the critical point in the initiation of the fracture due to the higher levels of η and $\bar{\varepsilon}_{eq}$. The histories were recovered until the instant of fracture initiation, characterized by the point on the experimental engineering stress-strain curves where the stress capacity is

abruptly lost [3], as indicated in Fig. 5. With the parameters $\bar{\varepsilon}_f$, η and $\bar{\theta}$ for the three tests, the MMC criterion calibration was performed by using a nonlinear fitting tool available in Matlab software, obtaining the coefficients $c_1 = 0.139$, $c_2 = 331.7$ and $c_3 = 0.613$. The Fig. 6 shows the fracture initiation surface defined by MMC. The tests used for fracture calibration are highlighted.

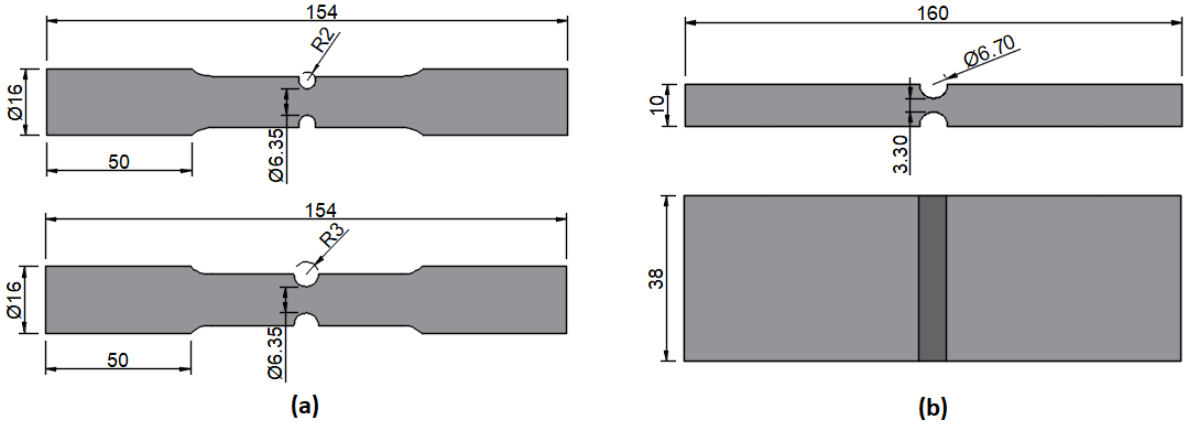

Figure 3. Main dimensions of the tested specimens (a) NRB (b) FGP

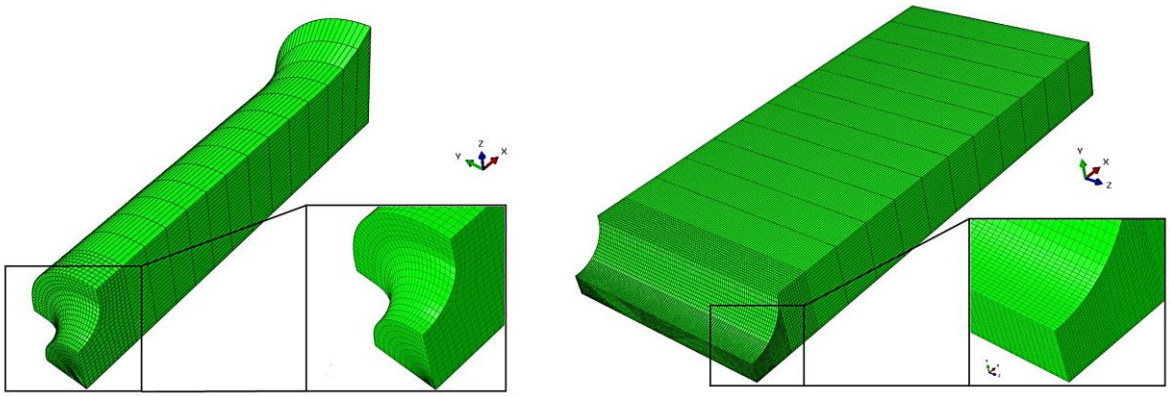

Figure 4. Mesh in finite element of the specimens tested

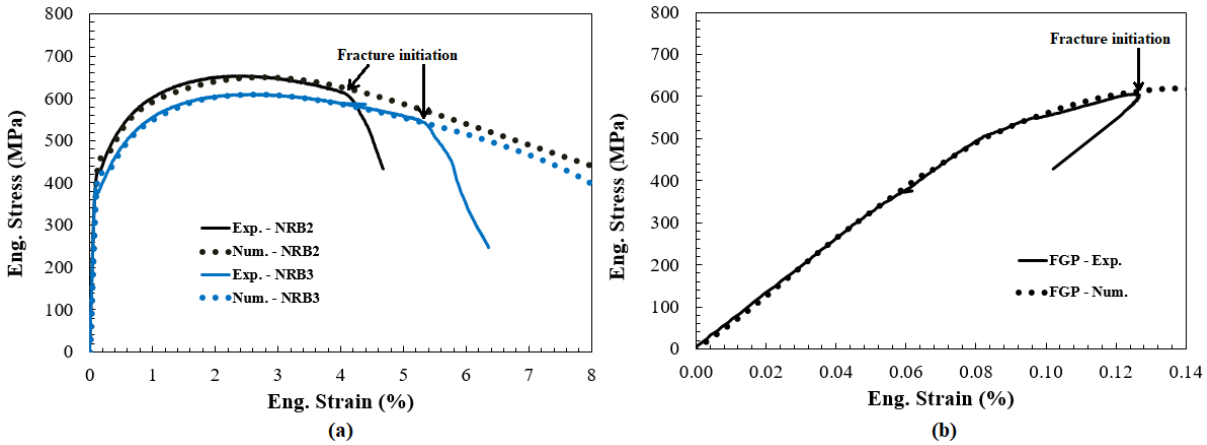

Figure 5. Engineering stress-strain curves (a) NRB (b) FGP

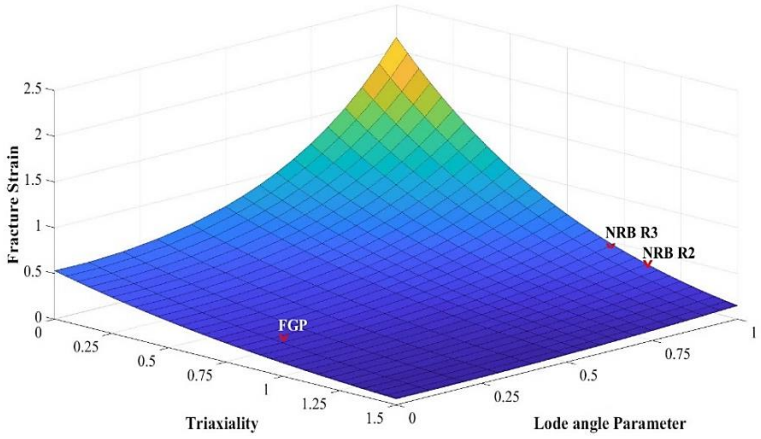

Figure 6. Surface representation of MMC fracture initiation criterion for ASTM A285

4.3 Softening law calibration

The damage evolution law coefficients calibration was performed using the load-crack mouth opening displacement curves (P-CMOD) obtained from small scale fracture tests of three-point bending specimens [SE(B)]. The Fig. 7a shows the settings of these tests. Two specimens were tested, both with $W = 19\ mm$, $B = W$, and $S = 4W$. For the damage evolution law coefficients calibration, a specimen with $a/W = 0.5$ (deep crack) were used, while the other specimen with $a/W = 0.2$ (shallow crack) was used for verification purpose of the calibrated parameters. Both specimens are provided with side-grooves. FE model was built with only $1/4$ of geometry with its boundary conditions imposed to the respective symmetry planes. C3D8R elements were used in the simulations, with a mesh refinement in the crack region. Fig. 7b shows the FE model constructed for the SE(B) with deep crack.

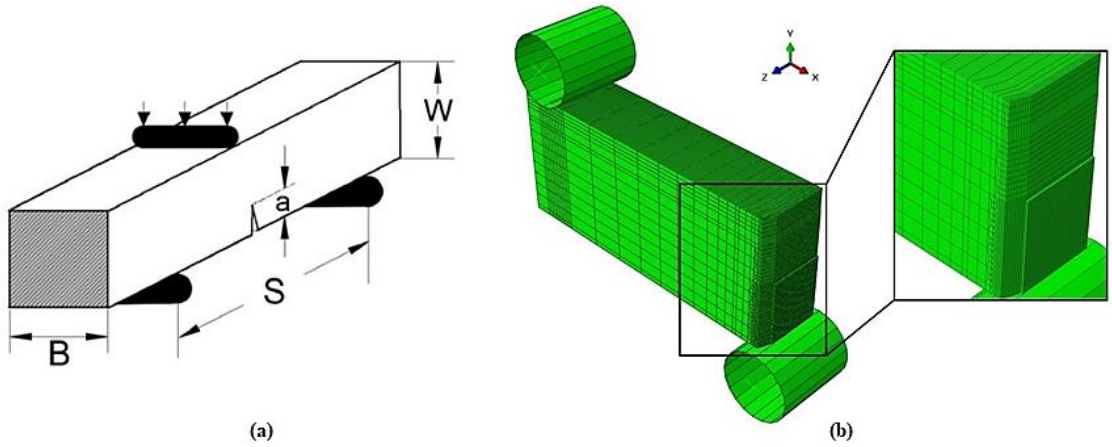

Figure 7. SE(B) specimen (a) test settings and main dimensions [8] (b) FE mesh SE(B) deep crack

The damage variable D is calculated according to the exponential softening law presented in Eq. 11, requiring the obtaining of two coefficients: $\bar{u}_f^{pl}$ and m. The adopted calibration procedure consists of performing iterations between the values of the two coefficients, in order to reproduce the P-CMOD curve of the SE(B) with $a/W = 0.5$ [10]. The values $\bar{u}_f^{pl} = 0.17$ and $m = 0.50$ satisfy the condition. The graphs presented in the Fig. 8a compares the experimental and numerical curves. The numerical model was able to recover the experimental curves by adopting these values for the coefficients. However, when performing the analysis without defining the softening law, the numerical curve was unable to predict the correct behavior of the test. Fig. 8b compares the experimental and numerical P-CMOD curves for the shallow cracked SE(B) specimen. The agreement is good, which validates the adopted numerical procedure for defining the model damage parameters.

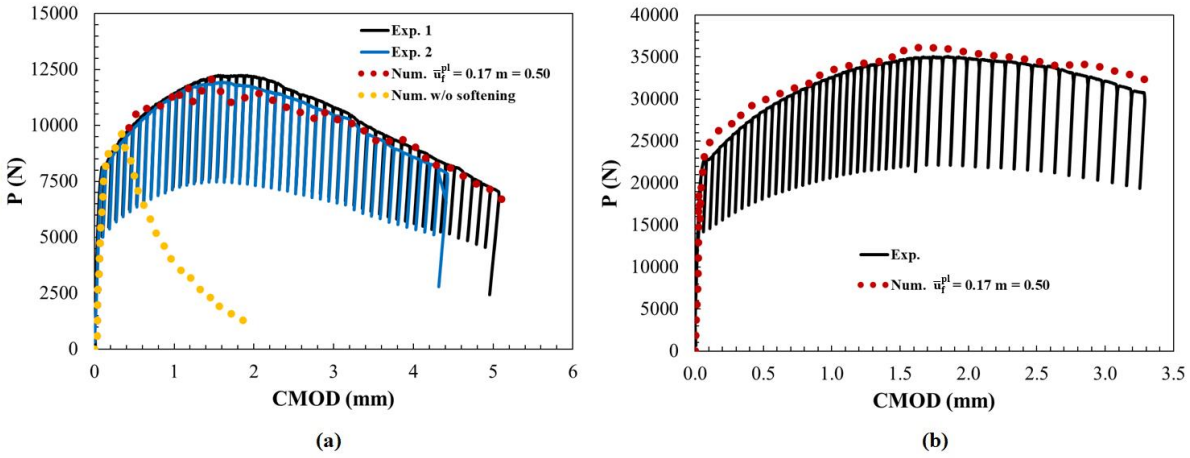

Figure 8. P-CMOD curves SE(B) tests (a) $a/W = 0.5$ (b) $a/W = 0.2$

5 Conclusions

It was presented the calibration process of a phenomenological model composed of a fracture initiation criterion coupled with a material softening law after fracture initiation. Experimental tests were performed in notched round bars, flat grooved plates, and bending specimens for the model coefficients calibration. 3D nonlinear finite element analyses were conducted to obtain the stress and strain histories at the critical points of the NRB and FGP and the consequent calibration of the modified Mohr-Coulomb criterion used to indicate fracture initiation. The softening law coefficients were obtained with analyzes reproducing the P-CMOD curves for the SE(B) with deep crack. Another test of a SE(B) with shallow crack was performed to validate the damage model, which was able to predict the ductile fracture of the specimen.

Acknowledgements. The authors thank the Coordination for the Improvement of Higher Education Personnel (CAPES) and the Department of Naval and Oceanic Engineering of the University of São Paulo for providing the necessary means to develop this research.

Authorship statement. The authors hereby confirm that they are the sole liable persons responsible for the authorship of this work, and that all material that has been herein included as part of the present paper is either the property (and authorship) of the authors, or has the permission of the owners to be included here.

References

[1] L. Xue and Xue Liang, "Ductile fracture modeling: theory, experimental investigation and numerical verification," *PhD Thesis*, no. January 2009, p. 251, 2007.
[2] J. Paulo, M. Brito, P. Marta, and C. Cardoso, "Ductile Fracture Prediction Using a Coupled Damage Model," 2018.
[3] R. Kiran and K. Khandelwal, "Experimental studies and models for ductile fracture in ASTM A992 steels at high triaxiality," *J. Struct. Eng. (United States)*, vol. 140, no. 2, pp. 1–11, 2014, doi: 10.1061/(ASCE)ST.1943-541X.0000828.
[4] A. Mendelson, *Plasticity : Theory and Application*. 1983.
[5] Y. Bai and T. Wierzbicki, "A new model of metal plasticity and fracture with pressure and Lode dependence," *Int. J. Plast.*, vol. 24, no. 6, pp. 1071–1096, 2008, doi: 10.1016/j.ijplas.2007.09.004.
[6] Y. Bai and T. Wierzbicki, "Application of extended Mohr-Coulomb criterion to ductile fracture," *Int. J. Fract.*, vol. 161, no. 1, pp. 1–20, 2010, doi: 10.1007/s10704-009-9422-8.
[7] Simulia, *Abaqus / CAE 6.14 User's Manual*. 2014, pp. 1–1146.
[8] C. A. Cuenca and D. F. B. Sarzosa, "Modeling ductile fracture using critical strain locus and softening law for a typical pressure vessel steel," *Int. J. Press. Vessel. Pip.*, vol. 183, no. March, p. 104081, 2020, doi: 10.1016/j.ijpvp.2020.104081.
[9] T. Wierzbicki, Y. Bao, Y. W. Lee, and Y. Bai, "Calibration and evaluation of seven fracture models," *Int. J. Mech. Sci.*, vol. 47, no. 4-5 SPEC. ISS., pp. 719–743, 2005, doi: 10.1016/j.ijmecsci.2005.03.003.
[10] M. Paredes, D. F. B. Sarzosa, R. Savioli, T. Wierzbicki, D. Y. Jeong, and D. C. Tyrell, "Ductile tearing analysis of TC128 tank car steel under mode I loading condition," *Theor. Appl. Fract. Mech.*, vol. 96, no. September 2017, pp. 658–675, 2018, doi: 10.1016/j.tafmec.2017.10.006.